Chemical Science

ROYAL SOCIETY OF CHEMISTRY

EDGE ARTICLE

View Article Online
View Journal

Cite this: DOI: 10.1039/d5sc09543c

All publication charges for this article have been paid for by the Royal Society of Chemistry

Pd-N-C shelled Pd nanoparticle catalysts for high-performance hydrogen peroxide electrosynthesis

Jiao Dong,†[a] Zixiang Su,†[bc] Yanyan Jia,†[d] Runjia Xing,†[a] Sixuan She,[e] Daqin Guan,[f] Sheng Dai,[d] Jinling Wang,[a] Manqing Chai,[a] Zhenshan Hou,[a] Zhi-Qiang Wang,*[a] Hehe Wei,*[a] P. Hu[ag] and Xue-Qing Gong*[b]

Received 5th December 2025
Accepted 7th April 2026

DOI: 10.1039/d5sc09543c

rsc.li/chemical-science

Metal-nitrogen-carbon (M-N-C) catalysts have attracted widespread attention due to their potential in promoting the electrochemical oxygen reduction reaction (ORR) for the selective production of hydrogen peroxide (H_2O_2). However, the effects of their diverse structures and complex compositions on the catalytic performance remain poorly understood. Herein, systematic theoretical calculations reveal that the Pd-N-C based single-atom catalyst featuring a 1 : 1 ratio of pyridinic and pyrrolic nitrogen adopts a centrosymmetric PdN_4 structure ($Pd_{SA}N_{2\text{-}2}C$), and the Pd d_{z^2} orbital can strongly interact with the O 2p orbital of the adsorbed OOH intermediate, thereby strengthening its adsorption and facilitating subsequent conversion to H_2O_2. Guided by the theoretical insights, the $Pd_{SA}N_{2\text{-}2}C$ catalyst and a novel $Pd@Pd_{SA}N_{2\text{-}2}C$ core–shell catalyst with Pd nanoparticles encapsulated by an ultrathin $Pd_{SA}N_{2\text{-}2}C$ shell are synthesized, and the latter exhibits a remarkable H_2O_2 selectivity of 97% and a high yield of 35.88 mol g_{cat}^{-1} h^{-1} at an industrially relevant current density of 200 mA cm^{-2}, along with superior operational stability. This combined theoretical and experimental study provides useful guidance for the rational design of high-efficiency M-N-C catalysts for selective electrocatalysis.

Introduction

Nitrogen-modified-carbon supported metal single-atom catalysts (M-N-C) have shown significant promise for the oxygen reduction reaction (ORR) owing to their structural tunability,[1–3] excellent electrical conductivity and low cost.[4–8] The varying types of nitrogen coordination (such as pyridinic, pyrrolic and graphitic nitrogen) as well as the electronic properties of the active metal sites in M-N-C catalysts are expected to be critically important for the two-electron ($2e^-$) ORR toward hydrogen peroxide (H_2O_2) production.[9–11] In particular, significant research efforts have been dedicated to elucidating how the pyridinic- and pyrrolic-nitrogen coordination environments affect the active sites and enhance the catalytic selectivity toward the $2e^-$ ORR.[12–16] Through combined theoretical and experimental studies, Chen *et al.* reported that pyrrole-type CoN_4 single atom catalysts exhibit a remarkable H_2O_2 selectivity of 94% at 0.3 V *versus* the reversible hydrogen electrode (*vs.* RHE) in a flow cell,[12] and it was mainly attributed to the increased adsorption strength of OOH, the key intermediate species for H_2O_2 formation, as a result of charge redistribution among the multiple d orbitals of Co after its adsorption. In contrast, Wang *et al.* found that pyridine-type CoN_4 catalysts exhibit a much lower H_2O_2 selectivity of only 29% at 0.4 V *vs.* RHE. This decrease in selectivity was potentially attributed to the modulation of the metal center by pyridinic N, which leads to strong H_2O_2 adsorption and subsequent dissociation.[13] Although these studies illustrated that pyrrole-type M-N-C single-atom catalysts generally exhibit higher $2e^-$ ORR selectivity than pyridine-type catalysts, the synergistic effects of different nitrogen coordination environments on the active metal center remain elusive, and the related catalytic mechanisms are also controversial.[11–19]

Beyond nitrogen coordination, the selection of the metal center is another crucial determinant of $2e^-$ ORR selectivity and

[a]State Key Laboratory of Green Chemical Engineering and Industrial Catalysis, Center for Computational Chemistry and Research Institute of Industrial Catalysis, School of Chemistry and Molecular Engineering, East China University of Science and Technology, 130 Meilong Road, Shanghai, 200237, China. E-mail: zhiqiangwang@ecust.edu.cn; weihh@ecust.edu.cn

[b]State Key Laboratory of Synergistic Chem-Bio Synthesis, School of Chemistry and Chemical Engineering, Shanghai Jiao Tong University, 800 Dongchuan Road, Shanghai, 200240, China. E-mail: xqgong@sjtu.edu.cn

[c]National Engineering & Technology Research Center of Scattered Metals, First Rare Materials Co., Limited, Baijia Industrial Park 27-9B, Qingyuan, Guangdong, 511517, China

[d]Key Laboratory for Advanced Materials and Feringa Nobel Prize Scientist Joint Research Center, School of Chemistry and Molecular Engineering, East China University of Science and Technology, 130 Meilong Road, Shanghai, 200237, China

[e]Department of Applied Physics, The Hong Kong Polytechnic University, Hung Hom, Kowloon, Hong Kong SAR, China

[f]WA School of Mines: Minerals, Energy and Chemical Engineering (WASM-MECE), Curtin University, Perth, WA 6102, Australia

[g]School of Physical Science and Technology, Shanghai Tech University, 393 Middle Huaxia Road, Shanghai, 201210, China

† These authors contributed equally.

activity. Several studies have demonstrated that atomically dispersed metal centers coordinated with nitrogen-doped carbon matrices may exhibit distinct catalytic performances in H_2O_2 production. Notably, it has been suggested that single-atom Pd-N-C catalysts are highly efficient for the $2e^-$ ORR to H_2O_2.[18–21] For example, Jiang *et al.* synthesized a series of single atom catalysts including Pd-N-C, Co-N-C, and Mn-N-C, and they demonstrated that the corresponding H_2O_2 selectivity at 0.82 V *vs.* RHE was 90.3%, 74.8% and 39.8% for these catalysts, respectively.[18] Wang *et al.* confirmed the outstanding performance of the single-atom Pd-N-C catalyst, which achieved approximately 95% H_2O_2 selectivity and an onset potential of ~0.8 V *vs.* RHE.[19] Generally, these findings underscored that both the local nitrogen coordination environment and the identity of the active metal center can tailor the $2e^-$ ORR performance. Notably, under alkaline conditions, the $2e^-$ ORR usually exhibits enhanced activity and selectivity towards H_2O_2 due to the pH effect,[22,23] which can help optimize the intermediate adsorption strength[24] as well as the thermodynamics of ORR processes.[25] Therefore, unraveling the distinct nitrogen coordination motifs and electronic characteristics of catalytic centers at the atomic level is imperative for enabling efficient H_2O_2 electrosynthesis under industrially relevant alkaline conditions.

In this work, by using integrated density functional theory (DFT) calculations and experimental investigations, we elucidated the atomic-level interplay between nitrogen coordination symmetry and d-orbital engineering in Pd-N-C catalysts for highly efficient H_2O_2 production *via* the $2e^-$ ORR. Our calculated results revealed a synergistic modulation mechanism where a balanced 1 : 1 ratio of pyridinic to pyrrolic N coordination induces a centrosymmetric PdN_4 structure and promotes coupling between the Pd d_{z^2} orbital and the 2p orbital of the terminal O atom (O_T) of the OOH species binding with Pd through such O_T. This configuration enhances OOH adsorption and reduces the $2e^-$ ORR overpotential (η) to 0.54 V, which is significantly lower than that of previously reported Pd-N-C catalysts (η = 0.77 V).[19] Guided by the theoretical insights, we employed a dynamic coordination and selective etching (DC–SE) approach for the syntheses of atomically dispersed Pd sites with targeted nitrogen coordination ratios and an interface-constrained self-assembly (ICSA) strategy for the construction of a novel core–shell type catalyst featuring metallic Pd core encapsulated by an ultrathin (~1.0 nm) N-coordinated Pd shell with a 1 : 1 coordination of pyridinic and pyrrolic nitrogen ($Pd@Pd_{SA}N_{2\text{-}2}C$). The $Pd@Pd_{SA}N_{2\text{-}2}C$ catalyst delivered exceptional H_2O_2 electrosynthesis performance with a remarkable selectivity of 97%. Moreover, it delivered a high H_2O_2 yield of 35.88 mol g_{cat}^{-1} h^{-1} at an industrially relevant current density of 200 mA cm^{-2} and produced 34.27 g L^{-1} H_2O_2 within 1080 min, demonstrating superior durability and thereby outperforming previously reported catalysts.[2,19,26–31] This work also provides valuable insights into designing high-performance single-atom catalysts through modulating atomic-level coordination symmetry and active-site orbital levels.

Methods

Computational methods

All the structural optimizations and total energy calculations in this work were performed with spin-polarized DFT by using the Vienna *Ab initio* Simulation Package (VASP).[32–35] The Perdew–Burke–Ernzerhof (PBE) functional within the generalized gradient approximation (GGA)[36,37] and the projector augmented wave (PAW) method[38,39] were applied throughout the geometric, electronic and energetic calculations. A cut-off energy of 400 eV was used, and the convergence criteria of energy and force in the calculations were set as 10^{-4} eV $Å^{-1}$ and 0.05 eV $Å^{-1}$, respectively.

For the construction of the $Pd_{SA}NC$ model catalyst, we built a $p(7 \times 7)$ single-layer graphene structure, where two adjacent C atoms were replaced with one Pd atom and four C atoms around the Pd atoms were further substituted with four N atoms, and one O was also included on the surface to form a C–O–C group. Both pyridinic N and pyrrolic N were considered. To model the core–shell structure of $Pd@Pd_{SA}N_{2\text{-}2}C$, we built the surface slab of Pd(111) covered by a $Pd_{SA}N_{2\text{-}2}C$ layer with minimal lattice mismatch. Specifically, the complex slab contains $p(9 \times 9)$ $Pd_{SA}N_{2\text{-}2}C$ and $p(8 \times 8)$ Pd(111), which were determined to give a lattice mismatch rate of 0.29%. Vacuum gaps of ~10 Å for $Pd_{SA}NC$ surfaces and ~20 Å for $Pd@Pd_{SA}N_{2\text{-}2}C$ surfaces were used to eliminate the interaction between neighboring slabs. The Brillouin zones were sampled with *k*-point meshes of 2 × 2 × 1 and 1 × 1 × 1 Gamma grids for $Pd_{SA}NC$ and $Pd@Pd_{SA}N_{2\text{-}2}C$ surfaces, respectively. The calculated ORR mechanisms and other computational details are provided in the SI.

Synthesis of core–shell $Pd@Pd_{SA}NC$ catalysts

The $Pd@Pd_{SA}NC$ catalysts were synthesized using an interface-constrained self-assembly strategy.[40] In a typical synthesis, 90 mL of ethanol, 45 mL of ultrapure water, and 0.45 mL of ethylenediamine were added to a 250 mL beaker and stirred at a rate of 560 rpm. for 30 min. Subsequently, 0.36 g of resorcinol was gently introduced into the above solution and stirred for another 30 min. Concurrently, 0.02 g of $Pd(acac)_2$ was dissolved in 10 mL of ethanol by ultrasonication at 40 °C. Subsequently, 0.45 mL of formaldehyde and the prepared Pd solution were added into the above beaker and stirred for 24 h at room temperature. The resulting precursors were collected through centrifugation, rinsed three times with ultrapure water and ethanol, and dried at 65 °C. Next, the dried precursors were placed in an alumina boat and pyrolyzed in a tube furnace under a constant N_2 flow at temperatures of 550 and 950 °C for 2 h to synthesize $Pd@Pd_{SA}N_{2\text{-}2}C$ and $Pd@Pd_{SA}N_{3\text{-}1}C$, respectively.

The $Pd_{SA}NC$ materials were synthesized by a dynamic coordination and selective etching process, which involved the co-condensation of Pd precursors (0.02 g $Pd(acac)_2$) with phenolic resin precursors (0.36 g resorcinol and 0.45 mL formaldehyde) and 0.45 mL ethylenediamine, followed by nitrogen-coordination-driven pyrolysis (550 and 950 °C for 2 h with a N_2 flow) and acid etching (50 mL nitrohydrochloric acid at 50 °C for 24 h), which finally generated $Pd_{SA}N_{2\text{-}2}C$ and $Pd_{SA}N_{3\text{-}1}C$, respectively. More details of synthesis are provided in the SI.

Electrochemical measurements

All electrochemical measurements were conducted on a CHI 760E electrochemical workstation at room temperature. The experimental setup comprised a RRDE, an Ag/AgCl reference electrode (saturated by KCl), and a graphite rod as the counter electrode. The RRDE assembly (IPS Elektroniklabor) consisted of a glass carbon rotating disk electrode (disk area of 0.196 cm^2) and a Pt ring (ring area of 0.159 cm^2). Notably, the experimentally determined apparent collection efficiency under the ferrocyanide/ferricyanide half-reaction system agreed well with the theoretical value of 34.4%. All potentials were calibrated to the RHE according to the equation $E_{RHE} = E_{Ag/AgCl} + 0.199V + 0.059 \times pH - iR \times 85\%$, where pH was measured using a pH meter.

For the preparation of catalytic ink, 4 mg of as-prepared catalyst and 1.5 mg of XC-72R were dispersed in a mixture containing 870 μL of isopropanol, 100 μL ultrapure water and 30 μL Nafion solution (5 wt%), followed by ultrasonication for 30 min to ensure a homogeneous dispersion. Then, 2.5 μL of ink was added dropwise onto the glassy carbon disk electrode and dried by rotating the electrode at 500 rpm, yielding a film-coated electrode.

The RRDE measurements were performed in O_2-saturated 0.1 M KOH aqueous solution, over a potential range from 1.1 to 0.1 V *vs.* RHE, at a scan rate of 10 mV s^{-1} and a rotation speed of 1600 rpm. During these measurements, the ring electrode was held at a constant potential of 1.2 V *vs.* RHE. Prior to each ORR test, the catalyst was activated by 30 cycles of potential cycling between 1.1 and 0.1 V *vs.* RHE at a scan rate of 50 mV s^{-1} in N_2-saturated 0.1 M KOH solution. Subsequently, the electrolyte was purged with O_2 for at least 30 min to ensure optimal ORR conditions. The LSV curves for the ORR were obtained by subtracting the currents measured in N_2-saturated 0.1 M KOH, effectively eliminating capacitive currents. The H_2O_2 reduction performance was tested in N_2-saturated 0.1 M KOH containing 10 mM H_2O_2. The stability of the as-prepared catalysts was recorded by current–time (*i*–*t*) chronoamperometric measurements at 0.1 V *vs.* RHE in O_2-saturated 0.1 M KOH at 1600 rpm. for 60 000 s. The H_2O_2 selectivity and the electron transfer number (*n*) were determined using the following equations:

$$H_2O_2\% = \frac{200I_R/N}{I_D + I_R/N} \quad (1)$$

$$n = \frac{4I_D}{I_D + I_R/N} \quad (2)$$

where I_D is the disk current, I_R is the ring current, and N is the current collection efficiency of the Pt ring.

Results and discussion

Theoretical exploration of $Pd_{SA}NC$ catalysts with specific N ratios for the $2e^-$ ORR

It is well known that the surface structure and composition of M-N-C catalysts, especially the ratio of pyridinic to pyrrolic N, can significantly influence their ORR activity.[11,16,18] Moreover, as shown in previous studies, the presence of surface O species (particularly in the form of C–O–C groups) may also improve the $2e^-$ ORR activity.[3,31,41–43] Therefore, in this work, we first constructed a Pd-N-C catalyst modified with four pyridinic N atoms and one adsorbed O atom and progressively replaced the pyridinic N with the pyrrolic one, *i.e.*, $Pd_{SA}N_{4\text{-}0}C$, $Pd_{SA}N_{3\text{-}1}C$, $Pd_{SA}N_{2\text{-}2}C$ and $Pd_{SA}N_{1\text{-}3}C$ (where 4-0, 3-1, 2-2 and 1-3 denote the numbers of pyridinic and pyrrolic N atoms, see Fig. 1a–d). For each $Pd_{SA}NC$ catalyst, multiple possible C–O–C configurations at different carbon sites were examined (Fig. S1–S4 and Tables S1–S4), and the thermodynamically most stable structure was selected for all subsequent calculations. Our calculations showed that the $Pd_{SA}N_{4\text{-}0}C$ structure exhibits a high degree of both axial and central symmetries. Then, the introduction of pyrrolic N effectively alters the surface symmetry, resulting in asymmetric $Pd_{SA}N_{3\text{-}1}C$ and $Pd_{SA}N_{1\text{-}3}C$ structures, while the $Pd_{SA}N_{2\text{-}2}C$ structure is still centrosymmetric around the Pd center. These differences in nitrogen ratios and surface symmetries can modulate the valence state of the single Pd atom. Specifically, the calculated density of states (DOS) (Fig. 1e) illustrated that the highest occupied energy levels are from the d_{z^2} orbital in the single-atom Pd of the various $Pd_{SA}NC$ catalysts, while the introduction of pyrrolic N can modify the d-orbital configurations of the single Pd atom by causing the disappearance of $d_{x^2-y^2}$ and the appearance of d_{xy} at high energy levels.

To investigate the activity and selectivity of the ORR on the $Pd_{SA}N_{4\text{-}0}C$, $Pd_{SA}N_{3\text{-}1}C$, $Pd_{SA}N_{2\text{-}2}C$ and $Pd_{SA}N_{1\text{-}3}C$ catalysts, we systematically calculated the Gibbs free energy changes (ΔG) for the key steps in both $2e^-$ and $4e^-$ ORR processes ($2e^-$ associative pathway: $O_2 + 2(H_2O + e^-) \rightarrow H_2O_2 + 2OH^-$; $4e^-$ associative pathway $O_2 + 4(H_2O + e^-) \rightarrow 2H_2O + 4OH^-$) on these catalysts (Fig. S5–S10). The computational details are presented in SI Methods: ORR mechanism and calculation details. It is widely accepted that the catalytic selectivity towards H_2O_2 formation over H_2O is critically governed by the thermodynamics of the key intermediates, and a key descriptor for predicting this selectivity is the Gibbs free energy of *O (ΔG(*O)).[44,45] This is because, to make H_2O_2 production thermodynamically favorable, the O–O bond scission for the surface *OOH intermediate must be suppressed, and this can be achieved when the ΔG(*O) is higher than 3.52 eV ($\Delta G_{H_2O_2}$).[44–47] Our results showed that the calculated ΔG(*O) values for the $Pd_{SA}NC$ catalysts are all higher than 3.52 eV (the corresponding ΔG(*O) values are 3.63, 4.24, 4.81 and 4.92 eV for $Pd_{SA}N_{4\text{-}0}C$, $Pd_{SA}N_{3\text{-}1}C$, $Pd_{SA}N_{2\text{-}2}C$ and $Pd_{SA}N_{1\text{-}3}C$, see Fig. S1), indicating high selectivity for H_2O_2 production on these catalysts. At the same time, it can be noticed that the steps with the maximum ΔG (ΔG_{max}) during the $2e^-$ ORR are identical at various $Pd_{SA}NC$ catalysts, *i.e.*, the potential determining step (PDS) is the first step: $O_2 + H_2O + e^- + * \rightarrow *OOH + OH^-$. The corresponding overpotentials (η) were calculated to be 1.25 V, 0.63 V, 0.54 V and 0.59 V for the $Pd_{SA}N_{4\text{-}0}C$, $Pd_{SA}N_{3\text{-}1}C$, $Pd_{SA}N_{2\text{-}2}C$ and $Pd_{SA}N_{1\text{-}3}C$ catalysts, respectively, clearly showing that $Pd_{SA}N_{2\text{-}2}C$ shows the highest $2e^-$ ORR activity (Fig. 1f).

To understand the differences in $2e^-$ ORR activity and selectivity among these $Pd_{SA}NC$ catalysts, we performed DOS and Bader charge analyses to investigate the adsorption of key intermediates during the reaction processes on these catalyst

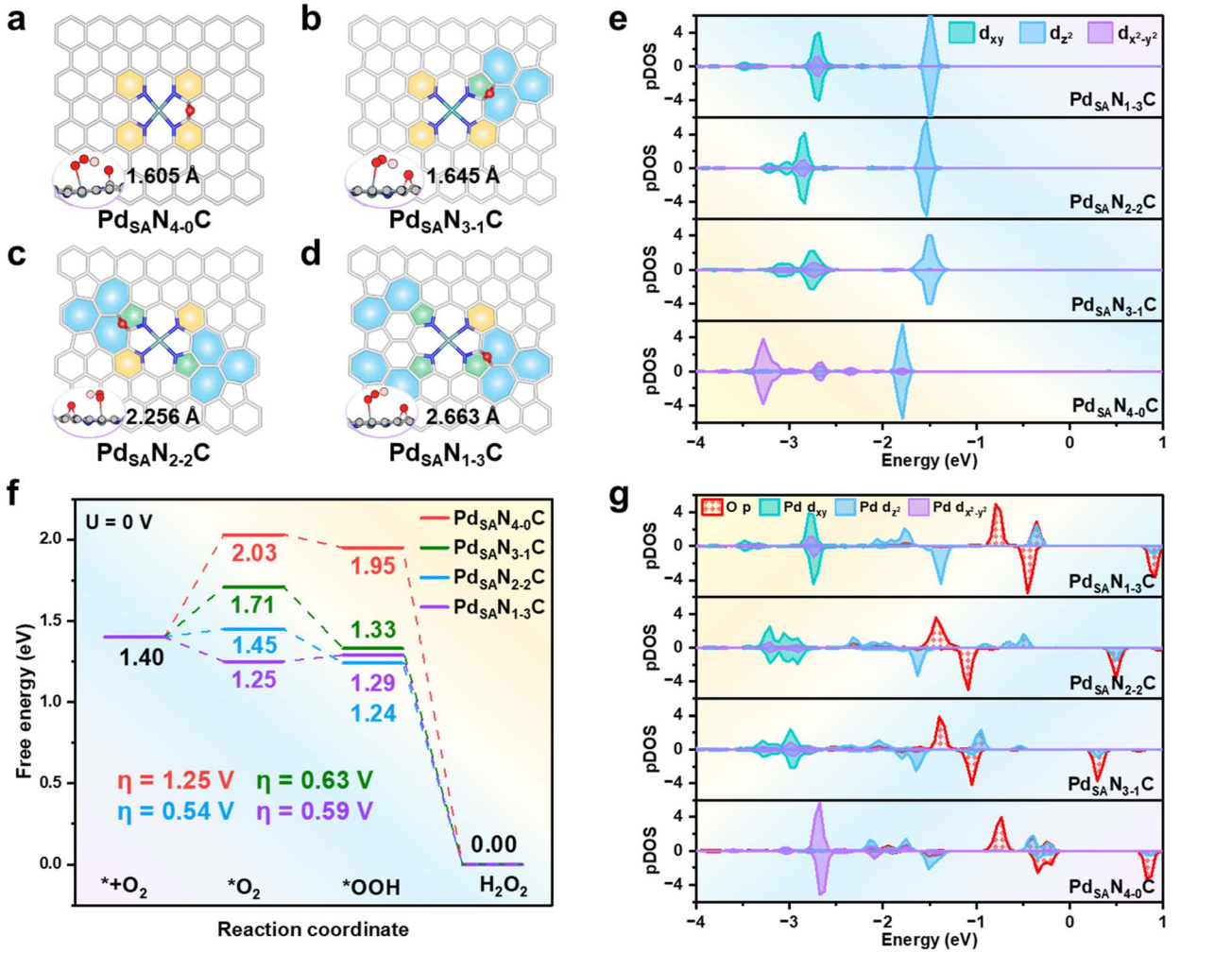

Fig. 1 DFT calculations of the ORR processes and electronic properties of various $Pd_{SA}NC$ catalysts. Calculated structures (top view) of (a) $Pd_{SA}N_{4\text{-}0}C$, (b) $Pd_{SA}N_{3\text{-}1}C$, (c) $Pd_{SA}N_{2\text{-}2}C$ and (d) $Pd_{SA}N_{1\text{-}3}C$ catalysts and those with OOH adsorption (inset: side view). Green: Pd, blue: N, red: O, grey: C, and pale pink: H. Hydrogen bonds are shown in the diagram. (e) Calculated partial density of states (pDOSs) of the split d orbitals of Pd single atoms at various $Pd_{SA}NC$ catalysts. (f) Calculated free energy profiles of the $2e^-$ ORR pathway and the corresponding overpotentials of different catalysts. (g) Calculated pDOSs of the p orbitals of O_T in *OOH and split d orbitals of Pd single atoms of $Pd_{SA}NC$ catalysts. All DOSs were aligned with respect to the 2s orbital of one specific C atom in the complete hexagonal ring of the catalysts.

surfaces. The calculated results revealed that on all the $Pd_{SA}NC$ catalysts, the *OOH intermediate binds to the Pd sites (with the O atom directly bonding with Pd being defined as O_T). Although a weak hydrogen-bond interaction between the H atom in *OOH and the O atom in the C–O–C group can help stabilize *OOH, this effect is common to all $Pd_{SA}NC$ catalysts, and the C–O–C group does not alter the Bader charge of the Pd center (Fig. 1a–d, S11 and S12). The stability of the resulting Pd–O_T bond mainly originates from electron transfer from the d_{z^2} orbital of Pd to the O_T 2p orbital (see Fig. 1e and g and S10 and Tables S5 and S6). The amount of electron transfer in this process follows the order: $Pd_{SA}N_{2\text{-}2}C > Pd_{SA}N_{1\text{-}3}C > Pd_{SA}N_{3\text{-}1}C \approx Pd_{SA}N_{4\text{-}0}C$ (with transferred charges calculated to be 0.225, 0.159, 0.103 and 0.108 |e|, respectively, see Table S5). In addition, we also found that on the surfaces where both pyridinic- and pyrrolic-N exist, in comparison with the $Pd_{SA}N_{4\text{-}0}C$ surface, the energy level of the d_{xy} orbital is lowered upon OOH adsorption, which may further indicate the enhancement of OOH adsorption.

Furthermore, we observed that as the content of pyrrolic N increases, the calculated Bader charge on the single atom Pd becomes more positive (0.709, 0.702, 0.712, and 0.741 |e| for $Pd_{SA}N_{4\text{-}0}C$, $Pd_{SA}N_{3\text{-}1}C$, $Pd_{SA}N_{2\text{-}2}C$ and $Pd_{SA}N_{1\text{-}3}C$, respectively, see Fig. S13). It clearly showed that a moderate (neither too high nor too low) positive Bader charge on the Pd site is favorable for OOH adsorption. Nevertheless, the $Pd_{SA}N_{2\text{-}2}C$ surface still exhibits the largest Bader charge change for the Pd after OOH adsorption, reaching 0.119 |e| (Fig. S13). Finally, we further calculated the electrostatic interaction energies (E_{inter}) between the O_T atom of the adsorbed OOH species and the Pd active site, which again confirms that the $Pd_{SA}N_{2\text{-}2}C$ surface interacts most strongly with the *OOH species (E_{inter} values for $Pd_{SA}N_{4\text{-}0}C$, $Pd_{SA}N_{3\text{-}1}C$, $Pd_{SA}N_{2\text{-}2}C$ and $Pd_{SA}N_{1\text{-}3}C$ are −1.27 eV, −1.28 eV, −1.50 eV and −1.35 eV, respectively, see Table S7), in excellent

agreement with the calculated 2e$^-$ ORR activity of the $Pd_{SA}NC$ catalysts.

Interestingly, our results can reveal a direct linear correlation between electron transfer and electrostatic interaction across the different $Pd_{SA}NC$ configurations: systems exhibiting larger electron transfer consistently display stronger electrostatic interactions (Fig. S14). Specifically, different N-coordination environments modulate the energy level distribution of Pd d-orbitals; the resulting changes further tune the ability of Pd to transfer electrons to *OOH, thereby strengthening the electrostatic interaction between Pd and the terminal O atom (O_T) in *OOH and ultimately governing the adsorption strength of *OOH. From the above discussion, we can conclude that the centrosymmetric $Pd_{SA}N_{2\text{-}2}C$ surface, with its balanced pyridinic-to-pyrrolic N ratio, can regulate the d-orbital distribution of the Pd center to transfer more electrons and achieve stronger electrostatic stabilization and help it maintain a moderate Bader charge, thereby facilitating OOH adsorption and leading to excellent 2e$^-$ ORR catalytic activity.

Syntheses and characterization of novel Pd-N-C catalysts

Inspired by the theoretical predictions of the optimal nitrogen coordination ratio for the electrochemical synthesis of hydrogen peroxide *via* the 2e$^-$ ORR, we tentatively synthesized two prototypical single-atom $Pd_{SA}NC$ catalysts, $Pd_{SA}N_{2\text{-}2}C$ (with high activity) and $Pd_{SA}N_{3\text{-}1}C$ (with low activity), both featuring the coexistence of pyridinic and pyrrolic nitrogen species. To rationally engineer these $Pd_{SA}NC$ catalysts, we developed two distinct synthetic strategies. Firstly, a dynamic coordination and selective etching approach[40] was used to construct these single-atom $Pd_{SA}NC$ catalysts with atomically dispersed Pd-N sites and tunable pyridinic-to-pyrrolic N distributions. Transmission electron microscopy (TEM) and high-angle annular dark-field scanning transmission electron microscopy (HAADF-STEM) images confirmed the atomic dispersion of Pd in the as-prepared $Pd_{SA}NC$ catalysts (Fig. S15–S17). X-ray photoelectron spectroscopy (XPS) analysis revealed that the $Pd_{SA}N_{2\text{-}2}C$ and $Pd_{SA}N_{3\text{-}1}C$ catalysts synthesized in this way indeed possess optimized pyridinic-to-pyrrolic nitrogen ratios of 1 : 1 and 3 : 1, respectively (Fig. S18). Notably, the $Pd_{SA}N_{2\text{-}2}C$ catalyst exhibited approximately 64% higher ring current (i_{ring}) and 16% higher disk current density (j_{disk}) than $Pd_{SA}N_{3\text{-}1}C$, with these performance enhancements being consistently observed across a broad potential window ranging from 0.3 to 0.6 V *vs.* RHE. Furthermore, $Pd_{SA}N_{2\text{-}2}C$ exhibited exceptional electrocatalytic performance, with a hydrogen peroxide selectivity close to 93% and an electron transfer number (n) of 2.2, which is also a significant improvement over $Pd_{SA}N_{3\text{-}1}C$ (77% selectivity, n = 2.5) as evidenced by the rotating ring-disk electrode (RRDE) measurement (Fig. S19–S22). The general consistency between experimental results and theoretical calculations suggested that the nitrogen coordination engineering strategy for the construction of a centrosymmetric structure can potentially give rise to enhanced 2e$^-$ ORR activity and selectivity.

Secondly, an interface-constrained self-assembly strategy (Fig. 2a) was used to form a N-containing resin precursor on Pd, followed by pyrolysis under N_2 to generate a structure in which Pd nanoparticles are encapsulated by an ultrathin Pd-N-C shell. By varying the pyrolysis temperature, the pyridinic/pyrrolic N distribution in the shell can be tuned. Specifically, at relatively lower temperatures, pyrrolic-N in pentagonal ring structures is more readily retained within the forming carbon matrix. As the temperature increases, additional dehydrogenation and structural rearrangement favor the formation of thermodynamically more stable pyridinic-N sites in hexagonal rings, leading to a corresponding increase in the proportion of pyridinic-N. Intriguingly, the as-prepared catalyst gave the conformation with a $Pd_{SA}NC$ shell encapsulating the Pd nanoparticle; *i.e.*, a $Pd@Pd_{SA}NC$ core–shell architecture was obtained through this synthesis strategy (Fig. 2b–e). The TEM measurement revealed that the core–shell $Pd@Pd_{SA}NC$ catalysts exhibit a nanosphere morphology, showing Pd nanocrystals with an average size of 21.9 nm (Fig. 2b and S23–S25) encapsulated by a $Pd_{SA}NC$ shell with a thickness of 1.0 nm (Fig. 2c–e). The core–shell structure was further confirmed by HAADF-STEM images (Fig. S26 and S27). Moreover, the uniform distribution of Pd, N, O, and C atoms in the shell of $Pd@Pd_{SA}NC$ was evidenced by STEM energy dispersive X-ray spectroscopy (EDS) mapping (Fig. S28 and S29). Overall, these findings suggested that following an interface-constrained self-assembly strategy, the structural evolution of the catalyst mainly originates from the suppression of Pd aggregation mediated by oxygen-containing functional groups. This modulation also facilitates lattice matching between metallic Pd and graphitic carbon domains during pyrolysis, thus promoting the epitaxial growth of nitrogen-doped carbon shells.

Then, the electronic properties of the $Pd@Pd_{SA}NC$ catalysts were analyzed using XPS (Fig. 2f and S30–S35) and X-ray absorption spectroscopy (XAS). The deconvoluted C 1s XPS spectra revealed peaks at 284.8 eV (sp^2-hybridized C–C), 285.9 eV (C–O/C–N), 287.3 eV (C=O), 288.9 eV (COOH), and 290.7 eV (π–π*) (Fig. S33a). The peak positions for both $Pd@Pd_{SA}N_{2\text{-}2}C$ and $Pd@Pd_{SA}N_{3\text{-}1}C$ remained virtually unchanged, with their corresponding peak area ratios also showing no significant variation. Combined with the Raman spectra (Fig. S33b), the I_D/I_G values of $Pd@Pd_{SA}N_{2\text{-}2}C$ and $Pd@Pd_{SA}N_{3\text{-}1}C$ are both less than 1, indicating that the carbon defect contents of both are relatively low.[48–50] Therefore, we can expect that the main source of its 2e$^-$ ORR activity is not the carbon framework itself. The high-resolution N 1s XPS spectra of $Pd@Pd_{SA}N_{2\text{-}2}C$ (Fig. 2f) show three prominent subpeaks at 398.4, 399.6 and 400.9 eV, corresponding to pyridinic-, pyrrolic- and graphitic-N, respectively. The combined atomic content of pyridinic- and pyrrolic-N in $Pd@Pd_{SA}N_{2\text{-}2}C$ was determined to be 4.17 at%, with their atomic ratio approximating 0.8 (close to 1 : 1, see Fig S35 and Table S8). In contrast, $Pd@Pd_{SA}N_{3\text{-}1}C$ exhibited a ratio of 3 : 1 for these two nitrogen species. Hence, although the two $Pd@Pd_{SA}NC$ catalysts demonstrated a similar carbon shell with similar carbon species and carbon defects, accompanied by atomically dispersed Pd, the $Pd@Pd_{SA}N_{2\text{-}2}C$ and $Pd@Pd_{SA}N_{3\text{-}1}C$ catalysts featured distinctive functional moieties in the carbon shell, including pyridinic- and pyrrolic-N, with a ratio close to 1 : 1 and 3 : 1, respectively.

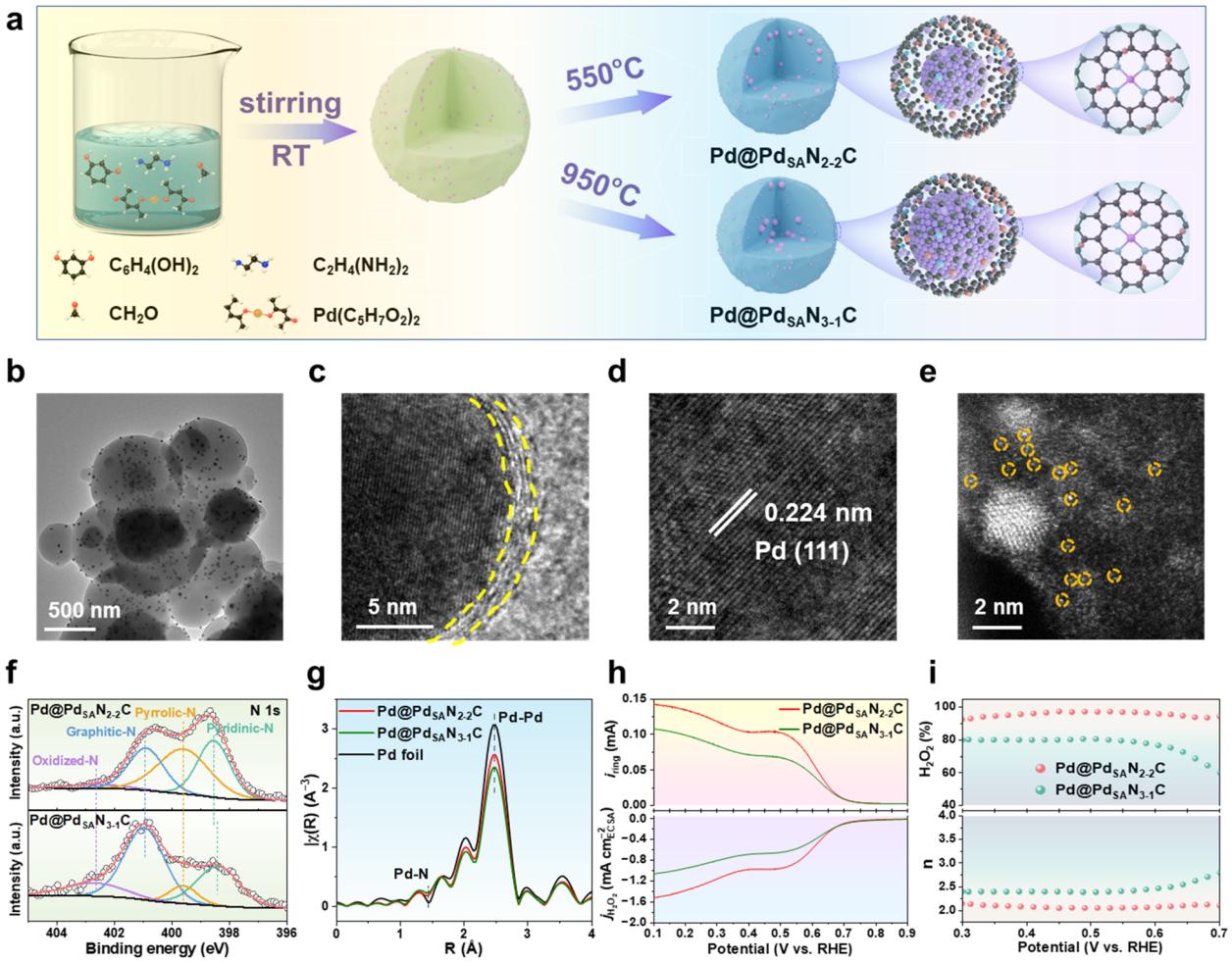

Fig. 2 Synthesis and characterization of Pd@Pd$_{SA}$NC catalysts. (a) Schematic illustration of the interface-constrained self-assembly strategy for the synthesis of Pd@Pd$_{SA}$NC. (b) TEM, (c and d) HRTEM and (e) STEM images of the Pd@Pd$_{SA}$N$_{2-2}$C catalyst. (f) XPS spectra of N 1s and (g) EXAFS spectra of Pd@Pd$_{SA}$NC catalysts. (h) Linear sweep voltammetry (LSV) curves of the ring current density and current density of H_2O_2 generation normalized by ECSA, and (i) H_2O_2 selectivity and electron transfer number of the ORR toward H_2O_2.

Complementary XAS results provided critical information on the Pd chemical states. In the X-ray absorption near-edge structure (XANES) analysis, the absorption edges of these Pd@Pd$_{SA}$NC catalysts shift to higher energy compared with the metallic Pd foil, indicating partially oxidized Pd (Fig. S36). Extended X-ray absorption fine structure (EXAFS) analysis further reveals a pronounced metal peak at ~2.5 Å, corresponding to Pd–Pd coordination (Fig. 2g), together with an additional feature at ~1.5 Å that can be assigned to the Pd–N coordination[1–3] (Fig. S37 and S38). It should be noted that because the bond lengths of Pd–N and Pd–O are nearly identical, structural assignment based solely on EXAFS fitting carries uncertainty. To further support the presence of Pd–N coordination, the color change observed during catalyst preparation and the UV-vis results (Fig. S39 and S40) were provided. These results indicated that, at the early stage of the liquid-phase synthesis, ethylenediamine effectively replaces the original acetylacetonate ligands and preferentially pre-coordinates with the Pd centers, thereby providing the basis for the formation of Pd–N coordination in the final catalyst. The fitted Pd–N coordination number is 3.89 (Table S9), suggesting the presence of Pd–N bonds within the PdN_4 structures. The integration of the morphological characterization and XPS analysis of Pd 3d gave compelling evidence for the existence of a core–shell structure, where the oxidized Pd species with nitrogen coordination constitute the Pd$_{SA}$NC shell, while the metallic Pd forms the encapsulated Pd nanoparticle core.[51]

Intriguingly, the H_2O_2 selectivity of Pd@Pd$_{SA}$N$_{2-2}$C was the highest among those of the various Pd$_{SA}$NC and Pd@Pd$_{SA}$N$_{3-1}$C catalysts, accompanied by significantly enhanced intrinsic activity (Fig. 2h and S20, S41–S46), indicating its superior ORR performance. Specifically, the Pd@Pd$_{SA}$N$_{2-2}$C catalyst achieved approximately 97% hydrogen peroxide selectivity and an electron transfer number of 2.1 across a very broad potential range from 0.3 to 0.7 V *vs.* RHE, outperforming those of previously reported catalysts[2,19,26–31] (Fig. 2i, S47 and S48, Table S10). Furthermore, RRDE measurement revealed that the Pd@Pd$_{SA}$N$_{2-2}$C catalyst also exhibited accelerated electron transfer kinetics and exceptional mass activity (Fig. S49 and S50). However, RRDE tests are often affected by O_2 diffusion. In

practical applications using a flow-cell measurement, which effectively overcomes the influence of mass transfer, it can be anticipated that Pd@$Pd_{SA}N_{2\text{-}2}C$ would achieve more efficient H_2O_2 synthesis.

Theoretical evidence for the high performance of Pd@Pd_{SA}NC in the 2e$^-$ ORR

To elucidate the reason for the enhanced 2e$^-$ ORR activity of the Pd@Pd_{SA}NC catalysts, we modeled and calculated the characteristic Pd@$Pd_{SA}N_{2\text{-}2}C$ structure with a minimal lattice mismatch rate of 0.29% (Table S11). It was constructed with a metallic Pd slab as the core covered by a Pd_{SA}NC single layer containing pyridinic and pyrrolic N at a 1 : 1 ratio (Fig. 3a). We then systematically calculated the Gibbs free energy changes for the key steps of the 2e$^-$ and 4e$^-$ ORR processes on this Pd@$Pd_{SA}N_{2\text{-}2}C$ catalyst (Fig. 3b and c, S51 and S52). The results showed that the ΔG(*O) on Pd@$Pd_{SA}N_{2\text{-}2}C$ is 4.36 eV (Fig. S52), which is greater than the benchmark of 3.52 eV,[44–47] indicating a preference for the 2e$^-$ ORR pathway and H_2O_2 production. We also found that the calculated η of such a core–shell Pd@$Pd_{SA}N_{2\text{-}2}C$ catalyst (η = 0.04 V) is much lower than that of the $Pd_{SA}N_{2\text{-}2}C$ catalyst (η = 0.54 V) and the Pd-N-C materials reported in the literature as well (η = 0.77 V),[19] which aligns well with our experimental results.

To further understand the fundamental reasons behind the high activity and selectivity of the Pd@$Pd_{SA}N_{2\text{-}2}C$ catalyst in the 2e$^-$ ORR process, we first carried out DOS calculations for the key intermediates on the surface. The results demonstrated that during the formation of the bond between the *OOH species and the single-atom Pd on the Pd@$Pd_{SA}N_{2\text{-}2}C$ surface, the electron occupation of the Pd d_{z^2} orbital is significantly reduced by 0.402 |e| (Fig. 3d), which is nearly twice that determined for the $Pd_{SA}N_{2\text{-}2}C$ catalyst (0.225 |e|, Table S5). Furthermore, Bader charge analysis revealed that, although the single atom Pd sites in both $Pd_{SA}N_{2\text{-}2}C$ and Pd@$Pd_{SA}N_{2\text{-}2}C$ catalysts possess similar Bader charges (0.712 and 0.718 |e|, respectively), the change in Bader charge of the shell Pd single atoms after OOH adsorption is more pronounced for the latter (0.119 and 0.125 |e| for $Pd_{SA}N_{2\text{-}2}C$ and Pd@$Pd_{SA}N_{2\text{-}2}C$, respectively, Fig. S53). Notably, further calculations revealed that the core Pd cluster also promotes the electrostatic interaction between the single-atom Pd site in the $Pd_{SA}N_{2\text{-}2}C$ shell and the O_T in *OOH (the corresponding electrostatic interaction energy is −2.43 eV, see Fig. S53). To further investigate the role of the metallic Pd core, we calculated the d-band center of Pd on the $Pd_{SA}N_{2\text{-}2}C$ and Pd@$Pd_{SA}N_{2\text{-}2}C$ surfaces, as well as that of the shell ($Pd_{SA}N_{2\text{-}2}$C(Pd@$Pd_{SA}N_{2\text{-}2}$C)) and the core (Pd(Pd@$Pd_{SA}N_{2\text{-}2}$C)) in Pd@$Pd_{SA}N_{2\text{-}2}C$. The results indicate that the single-atom Pd in the $Pd_{SA}N_{2\text{-}2}$C(Pd@$Pd_{SA}N_{2\text{-}2}$C) shell has the lowest d-band center (Table S12), suggesting that the metallic Pd core can modulate the d-band center of the surface single-atom Pd *via* charge transfer, thereby optimizing the OOH adsorption and enhancing the 2e$^-$ ORR performance of Pd@$Pd_{SA}N_{2\text{-}2}C$.

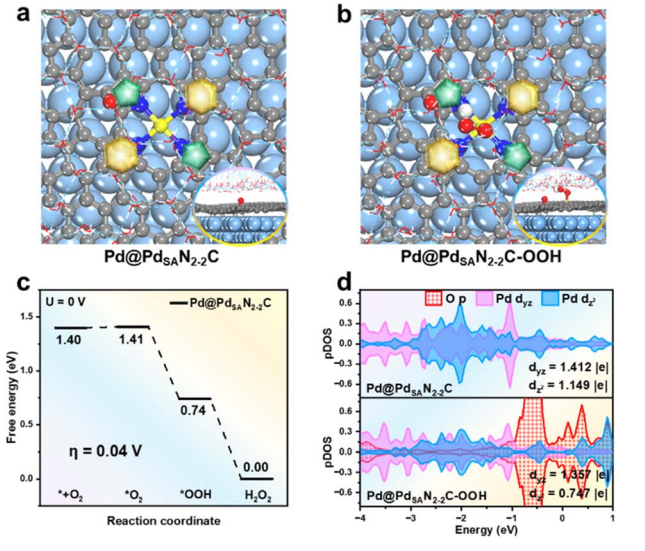

Fig. 3 Theoretical calculations of the ORR toward H_2O_2 formation at the Pd@$Pd_{SA}N_{2\text{-}2}C$ catalyst. (a) Calculated surface and (b) OOH adsorption structures of the Pd@$Pd_{SA}N_{2\text{-}2}C$ catalyst (top view; inset: side view). Yellow: Pd single atom, blue: N, red: O, white: H, grey: C, light blue: bulk Pd atoms, and red and white lines: H_2O molecules. (c) Calculated free energy profile of the 2e$^-$ ORR on the Pd@$Pd_{SA}N_{2\text{-}2}C$ surface. (d) Calculated pDOSs of the p orbital of O_T in *OOH and d orbitals of Pd single atoms in the Pd@Pd_{SA}NC catalyst shells.

Structure–activity relationship of the Pd@$Pd_{SA}N_{2\text{-}2}C$ catalyst

Detailed experimental tests were conducted to better illuminate the catalytic activity of the Pd@$Pd_{SA}N_{2\text{-}2}C$ catalyst. *In situ* attenuated total reflection Fourier-transform infrared spectra (ATR-FTIR) were obtained for the ORR process at various potentials ranging from 0.9 to 0.0 V *vs.* RHE, and they revealed three distinct peaks, where the peak at 1236 cm^{-1} corresponds to the O-O stretching of the adsorbed OOH, while the peaks at about 1397 cm^{-1} and 1457 cm^{-1} may originate from the adsorbed H_2O_2 and O_2, respectively (Fig. 4a). Most importantly, the intensity of the broad *OOH peak increased as the applied potential decreased from 0.9 to 0.0 V *vs.* RHE (Fig. 4b), confirming that the 2e$^-$ ORR pathway indeed occurs on the Pd@$Pd_{SA}N_{2\text{-}2}C$ surface.

In addition, to elucidate the effect of the Pd single atom within the Pd_{SA}NC shell on the ORR activity and selectivity, a comparative study was performed by utilizing commercial Pd/C and the Pd_{SA}NC catalysts. The results showed that the exposed Pd nanoparticles in commercial Pd/C mainly facilitate the 4e$^-$ ORR pathway (Fig. S54), while the abundant surface Pd single atoms in the Pd_{SA}NC shell of the Pd@$Pd_{SA}N_{2\text{-}2}C$ catalyst serve as key active sites to promote the ORR process for H_2O_2 production. This conclusion was further confirmed by the SCN$^-$ poisoning experiment. Upon the addition of 10 mM KSCN, the disk current density decreased immediately by 9.6% (Fig. S55), further indicating that the Pd species are the main catalytic sites. This is in line with the electronic properties illustrated by the theoretical calculations discussed earlier.

Furthermore, the long-term stability of the Pd@$Pd_{SA}N_{2\text{-}2}C$ catalyst was evaluated using chronoamperometry assessments at a constant potential of 0.1 V *vs.* RHE. Over 60 000 s of continuous 2e$^-$ ORR operation, both the disk and ring currents

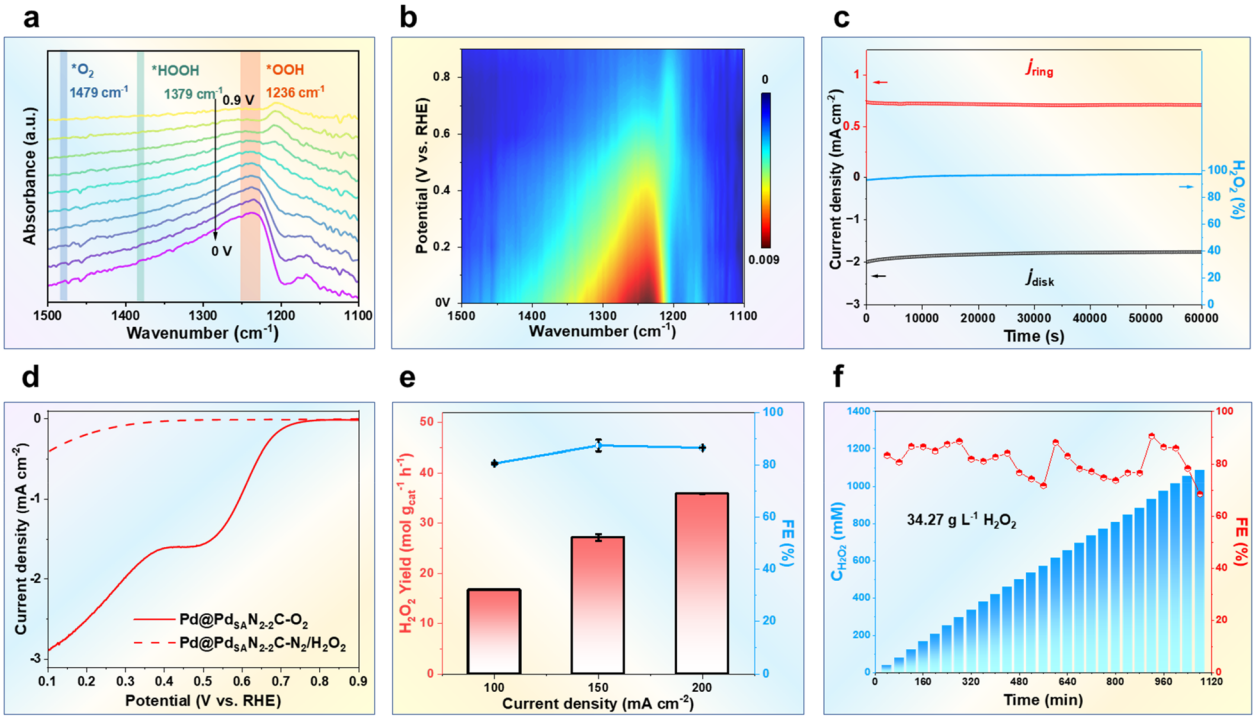

Fig. 4 Electrocatalytic 2e$^-$ ORR performance and mechanisms of the Pd@Pd$_{SA}$N$_{2\text{-}2}$C catalyst. (a and b) *In situ* ATR-SEIRAS spectra at different potentials from 0.9 to 0.0 V *vs.* RHE. (c) Stability at 0.3 V *vs.* RHE. (d) LSV curves of the H_2O_2RR and ORR. (e) H_2O_2 yields and faradaic efficiency (FE) at current densities from 100 to 200 mA cm^{-2}. (f) Continuous tests for H_2O_2 production for 1080 min at 200 mA cm^{-2}.

remained largely unchanged, and the H_2O_2 selectivity remained above 97% without any obvious decrease (Fig. 4c). The very small current density of the H_2O_2 reduction reaction (H_2O_2RR) observed in Pd@Pd$_{SA}$N$_{2\text{-}2}$C (Fig. 4d) indicated its negligible activity for the H_2O_2RR.

To rigorously assess the electrocatalytic performance of the Pd@Pd$_{SA}$N$_{2\text{-}2}$C catalyst for H_2O_2 synthesis under actual operating conditions, we conducted tests using an advanced three-phase flow cell setup (Fig. S56 and S57). The results further demonstrated that Pd@Pd$_{SA}$N$_{2\text{-}2}$C exhibited a high catalytic activity, with a H_2O_2 yield exceeding 15 mol g_{cat}^{-1} h^{-1} at current densities from 100 to 200 mA cm^{-2}. Specifically, the H_2O_2 yield of Pd@Pd$_{SA}$N$_{2\text{-}2}$C reached 35.88 mol g_{cat}^{-1} h^{-1} at 200 mA cm^{-2}, with a H_2O_2 Faradaic efficiency (FE) of 86.55% and a mass activity of 870 $A_{H_2O_2}$ g_{cat}^{-1}. Compared with those of most reported electrocatalysts, this result demonstrates the relatively superior performance of our material, particularly in terms of H_2O_2 yield (Fig. 4e and S58, Table S13). Notably, even in 1.0 M KOH, Pd@Pd$_{SA}$N$_{2\text{-}2}$C demonstrated a superior H_2O_2 formation activity of 50 mol g_{cat}^{-1} h^{-1} and a H_2O_2 FE of approximately 90% (Fig. S59). These results suggested that the core–shell Pd@Pd$_{SA}$N$_{2\text{-}2}$C catalyst with a 1 : 1 ratio of pyridinic to pyrrolic N indeed exhibits a remarkable H_2O_2 generation rate at industrially relevant current densities.

Moreover, the large-scale continuous productivity and electrochemical stability of Pd@Pd$_{SA}$N$_{2\text{-}2}$C were further evaluated in 0.1 M KOH at 200 mA cm^{-2}. During the test, the potential remained stable at around −0.1 V *vs.* RHE (Fig. S60), and the H_2O_2 FE remained higher than 80%. Continuous electrolysis at 200 mA cm^{-2} for 1080 min gave a sustained high H_2O_2 yield, achieving a concentration of up to 34.27 g L^{-1} (Fig. 4f). Post-test XRD patterns, TEM images and XPS spectra of the catalyst showed neglectable changes (Fig. S61–S64). These findings demonstrated that the Pd@Pd$_{SA}$N$_{2\text{-}2}$C catalyst can maintain excellent H_2O_2 generation performance even under scaled-up operation conditions, highlighting its superior efficacy and versatility.

Conclusions

In summary, we have systematically investigated the effects of local structures and nitrogen environments in Pd-N-C catalysts on the electrochemical 2e$^-$ ORR for H_2O_2 formation through combined theoretical and experimental studies. DFT calculation results revealed that the Pd$_{SA}$N$_{2\text{-}2}$C catalyst, featuring a 1 : 1 ratio of pyridinic to pyrrolic N atoms, exhibited superior activity for the 2e$^-$ ORR. This exceptional activity was attributed to the centrosymmetric structure of PdN_4 and the involvement of the d_{z^2} orbital of the single Pd atom in the formation of stable Pd-O bonds with the 2p orbital of O_T species in the adsorbed OOH intermediate. Furthermore, experimental efforts enabled the successful synthesis of both the Pd$_{SA}$N$_{2\text{-}2}$C catalyst and a complex one with a core–shell nanostructure, where the exposed two-dimensional structure involving atomically dispersed Pd atoms with tailored nitrogen coordination serves as the shell and the Pd nanoparticle as the core. The Pd@Pd$_{SA}$N$_{2\text{-}2}$C catalyst exhibited excellent 2e$^-$ ORR performance for H_2O_2 production, achieving a selectivity of 97% and a robust ring current across a broad potential window from 0.1 to 0.7 V *vs.* RHE in alkaline media. Our

calculated results further illustrated that the high performance of the Pd@$Pd_{SA}N_{2\text{-}2}C$ catalyst for the $2e^-$ ORR can be again attributed to the centrosymmetric PdN_4 structure in the shell, which maintains a structure similar to that of $Pd_{SA}N_{2\text{-}2}C$, as well as the existence of the Pd core that can modulate the d-orbital arrangement of the single Pd atom in the shell. Within a gas diffusion electrode integrated flow-cell setup, Pd@$Pd_{SA}N_{2\text{-}2}C$ achieved a high H_2O_2 yield of 35.88 mol g_{cat}^{-1} h^{-1} at 200 mA cm^{-2} with over 80% selectivity, alongside a cumulative H_2O_2 concentration of 34.27 g L^{-1} over 1080 min, surpassing previously reported metal single-atom electrocatalysts. This work not only provides a deeper understanding of the structural and electronic features of M-N-C materials in electrocatalytic reactions, but it also offers valuable guidance for the development of highly efficient electrocatalysts for H_2O_2 production.

Author contributions

The manuscript was written through contributions from all authors. All authors have given approval to the final version of the manuscript.

Conflicts of interest

The authors declare no competing financial interest.

Data availability

Supplementary information (SI): data related to the ORR mechanism, computational details, chemicals and reagents, physicochemical characterization and electrochemical tests. See DOI: https://doi.org/10.1039/d5sc09543c.

Acknowledgements

This work was supported by the National Key R&D Program of China (2024YFA1509901, 2023YFA1508500, and 2021YFA1500700) and the National Nature Science Foundation of China (22572049 and 22203030).

References

1 H. Liu, L. Jiang, Y. Sun, J. Khan, B. Feng, J. Xiao, H. Zhang, H. Xie, L. Li, S. Wang and L. Han, *Adv. Energy Mater.*, 2023, **13**, 2301223.
2 B. Yue, L. Lei, H. Xie, Y. Si, Q. Yang and X. Liu, *ACS Appl. Mater. Interfaces*, 2023, **15**, 33665–33674.
3 Q. Zhang, X. Tan, N. M. Bedford, Z. Han, L. Thomsen, S. Smith, R. Amal and X. Lu, *Nat. Commun.*, 2020, **11**, 4181.
4 D. Zhang, F. She, J. Chen, L. Wei and H. Li, *J. Am. Chem. Soc.*, 2025, **147**, 6076–6086.
5 H. T. Chung, D. A. Culle, D. Higgins, B. T. Snee, E. F. Holb, K. L. More and P. Zelenay, *Science*, 2017, **357**, 479–484.
6 K. Kumar, L. Dubau, F. Jaouen and F. Maillard, *Chem. Rev.*, 2023, **123**, 9265–9326.
7 L. Yan, P. Li, Q. Zhu, A. Kumar, K. Sun, S. Tian and X. Sun, *Chem*, 2023, **9**, 280–342.
8 H. Huang, M. Sun, S. Li, S. Zhang, Y. Lee, Z. Li, J. Fang, C. Chen, Y.-X. Zhang, Y. Wu, Y. Che, S. Qian, W. Zhu, C. Tang, Z. Zhuang, L. Zhang and Z. Niu, *J. Am. Chem. Soc.*, 2024, **146**, 9434–9443.
9 Z. Levell, S. Yu, R. Wang and Y. Liu, *J. Am. Chem. Soc.*, 2025, **147**, 603–609.
10 Y. Wang, R. Shi, L. Shang, G. I. N. Waterhouse, J. Zhao, Q. Zhang, L. Gu and T. Zhang, *Angew. Chem., Int. Ed.*, 2020, **59**, 13057–13062.
11 J. Gao and B. Liu, *ACS Mater. Lett.*, 2020, **2**, 1008–1024.
12 S. Chen, T. Luo, X. Li, K. Chen, J. Fu, K. Liu, C. Cai, Q. Wang, H. Li, Y. Chen, C. Ma, L. Zhu, Y.-R. Lu, T.-S. Chan, M. Zhu, E. Cortés and M. Liu, *J. Am. Chem. Soc.*, 2022, **144**, 14505–14516.
13 W. Wang, Y. Hu, P. Li, Y. Liu and S. Chen, *ACS Catal.*, 2024, **14**, 5961–5971.
14 N. Zhang, T. Zhou, M. Chen, H. Feng, R. Yuan, C. Zhong, W. Yan, Y. Tian, X. Wu, W. Chu, C. Wu and Y. Xie, *Energy Environ. Sci.*, 2020, **13**, 111–118.
15 B. Ni, P. Shen, G. Zhang, J. Zhao, H. Ding, Y. Ye, Z. Yue, H. Yang, H. Wei and K. Jiang, *J. Am. Chem. Soc.*, 2024, **146**, 11181–11192.
16 H. Xu, D. Cheng, D. Cao and X. C. Zeng, *Nat. Catal.*, 2024, **7**, 207–218.
17 J. Gao, H. Yang, X. Huang, S.-F. Hung, W. Cai, C. Jia, S. Miao, H. M. Chen, X. Yang, Y. Huang, T. Zhang and B. Liu, *Chem*, 2020, **6**, 658–674.
18 K. Jiang, S. Back, A. J. Akey, C. Xia, Y. Hu, W. Liang, D. Schaak, E. Stavitski, J. K. Nørskov, S. Siahrostami and H. Wang, *Nat. Commun.*, 2019, **10**, 3997.
19 N. Wang, X. Zhao, R. Zhang, S. Yu, Z. H. Levell, C. Wang, S. Ma, P. Zou, L. Han, J. Qin, L. Ma, Y. Liu and H. L. Xin, *ACS Catal.*, 2022, **12**, 4156–4164.
20 Y. L. Wang, S. Gurses, N. Felvey, A. Boubnov, S. S. Mao and C. X. Kronawitter, *ACS Catal.*, 2019, **9**, 8453–8463.
21 Z. Wei, B. Deng, P. Chen, T. Zhao and S. Zhao, *Chem. Eng. J.*, 2022, **428**, 131112.
22 T. Zhang, W. Wang, W. Liu, Z. Guo and J. Liu, *Nat. Commun.*, 2025, **16**, 5240.
23 T. Wu, M. Sun and B. Huang, *Mater. Today Energy*, 2019, **12**, 426e430.
24 J. S. Spendelow and A. Wieckowski, *Phys. Chem. Chem. Phys.*, 2007, **9**, 26542675.
25 S. C. Perry, D. Pangotra, L. Vieira, L.-I. Csepei, V. Sieber, L. Wang, C. P. León and F. C. Walsh, *Nat. Rev. Chem.*, 2019, **3**, 442–458.
26 B. Xia, Q. Huang, K. Wu, L. Jiang, M. Li, L. Yu, S. Ding, Z. Nie, D. Hua, J. Duan and S. Chen, *AIChE J.*, 2023, **69**, e18022.
27 R. Shen, R. Shen, W. Chen, Q. Peng, S. Lu, L. Zheng, X. Cao, Y. Wang, W. Zhu, J. Zhang, Z. Zhuang, C. Chen, D. Wang and Y. Li, *Chem*, 2019, **5**, 2099–2110.
28 Y. Sun, L. Silvioli, N. R. Sahraie, W. Ju, J. Li, A. Zitolo, S. Li, A. Bagger, L. Arnarson, X. Wang, T. Moeller, D. Bernsmeier, J. Rossmeisl, F. Jaouen and P. Strasser, *J. Am. Chem. Soc.*, 2019, **141**, 12372–12381.
29 J. Du, S. Jiang, R. Zhang, P. Wang, C. Ma, R. Zhao, C. Cui, Y. Zhang and Y. Kang, *ACS Catal.*, 2023, **13**, 6887–6892.

30 S. Zhang, Z. Tao, M. Xu, L. Kan, C. Guo, J. Liu, L. He, M. Du and Z. Zhang, *Small*, 2024, **20**, 2310468.
31 Q. Chang, P. Zhang, A. H. B. Mostaghimi, X. Zhao, S. R. Denny, J. H. Lee, H. Gao, Y. Zhang, H. L. Xin, S. Siahrostami, J. G. Chen and Z. Chen, *Nat. Commun.*, 2020, **11**, 2178.
32 G. Kresse and J. Furthmüller, *Phys. Rev. B:Condens. Matter Mater. Phys.*, 1996, **54**, 11169.
33 G. Kresse and J. Hafner, *Phys. Rev. B:Condens. Matter Mater. Phys.*, 1993, **47**, 558.
34 G. Kresse and J. Hafner, *Phys. Rev. B:Condens. Matter Mater. Phys.*, 1994, **49**, 14251.
35 G. Kresse and J. Furthmüller, *Comput. Mater. Sci.*, 1996, **6**, 15–50.
36 J. P. Perdew, J. A. Chevary, S. H. Vosko, K. A. Jackson, M. R. Pederson, D. J. Singh and C. Fiolhais, *Phys. Rev. B:Condens. Matter Mater. Phys.*, 1992, **46**, 6671.
37 M. P. Teter, M. C. Payne and D. C. Allan, *Phys. Rev. B*, 1989, **40**, 12255–12263.
38 P. E. Blöchl, *Phys. Rev. B:Condens. Matter Mater. Phys.*, 1994, **50**, 17953.
39 G. Kresse and D. Joubert, *Phys. Rev. B:Condens. Matter Mater. Phys.*, 1999, **59**, 1758–1775.
40 Z. Su, H. Wei, L. Zhang, H. Li, P. Liu, Z. Hou and X. Gong, *Electrochim. Acta*, 2023, **468**, 143180.
41 Y. Yuan, J. Ma, B. Kang and J. Y. Lee, *ACS Catal.*, 2025, **15**, 4039–4050.
42 C. Tang, L. Chen, H. Li, L. Li, Y. Jiao, Y. Zheng, H. Xu, K. Davey and S.-Z. Qiao, *J. Am. Chem. Soc.*, 2021, **143**, 7819–7827.
43 E. Jung, H. Shin, B.-H. Lee, V. Efremov, S. Lee, H. S. Lee, J. Kim, W. H. Antink, S. Park, K.-S. Lee, S.-P. Cho, J. S. Yoo, Y.-E. Sung and T. Hyeon, *Nat. Mater.*, 2020, **19**, 436–442.
44 X. Guo, S. Lin, J. Gu, S. Zhang, Z. Chen and S. Huang, *ACS Catal.*, 2019, **9**, 11042–11054.
45 Y. Zou, X. Guo, X. Bian, Y. Zhang, W. Lin, S. Huang, Z. Chen and K. Ding, *Appl. Surf. Sci.*, 2022, **592**, 153233.
46 X. Chen, H. Zhu, J. Zhu and H. Zhang, *Chem. Eng. J.*, 2023, **451**, 138998.
47 Q. Liu, X. Bian, S. Xie, W. Ruan, W. Chen, X. Guo and K. Ding, *Int. J. Hydrogen Energy*, 2024, **51**, 1413–1420.
48 Q. Wu, H. Zou, X. Mao, J. He, Y. Shi, S. Chen, X. Yan, L. Wu, C. Lang, B. Zhang, L. Song, X. Wang, A. Du, Q. Li, Y. Jia, J. Chen and X. Yao, *Nat. Commun.*, 2023, **14**, 6275.
49 H. Gong, L. Wei, S. Chen, Z. Chen, T. F. Jaramillo and Z. Bao, *Nano Res.*, 2023, **16**, 11556–11563.
50 J. Su, L. Jiang, B. Xiao, Z. Liu, H. Wang, Y. Zhu, J. Wang and X. Zhu, *Small*, 2024, **20**, 2310317.
51 S. Wei, A. Li, J.-C. Liu, Z. Li, W. Chen, Y. Gong, Q. Zhang, W.-C. Cheong, Y. Wang, L. Zheng, H. Xiao, C. Chen, D. Wang, Q. Peng, L. Gu, X. Han, J. Li and Y. Li, *Nat. Nanotechnol.*, 2018, **13**, 856–861.